LaTeX File (.tex, .sty, .cls, .bst, .bib) Click here to access/download;LaTeX File (.tex, .sty, .cls, .bst, .bib);STOKES_V15.tex

Dedicated to the memory of our Scripps colleague and friend, Ken Melville (1946-2019).

The contribution of high frequency wind-generated surface waves to the Stokes drift

Luc Lenain* and Nick Pizzo

Scripps Institution of Oceanography, La Jolla, California

**Corresponding author address:* Luc Lenain, Scripps Institution of Oceanography, 9500 Gilman Dr., La Jolla, CA 92093-0213.

E-mail: llenain@ucsd.edu

ABSTRACT

The effects of surface waves on upper ocean dynamics enter the wave-averaged primitive equations through the Stokes drift. Through the resulting upper ocean dynamics, Stokes drift is a catalyst for the fluxes of heat and trace gases between the atmosphere and ocean. However, estimates of the Stokes drift rely crucially on properly resolving the wave spectrum. In this paper, using state of the art spatial measurements (in-situ and airborne remote sensing) from a number of different field campaigns, with environmental conditions ranging from 2 to 13 ms^{-1} wind speed and significant wave height of up to 4 m, we characterize the properties of the surface wave field across the equilibrium and saturation ranges and provide a simple parameterization of the transition between the two regimes that can easily be implemented in numerical wave models. We quantify the error associated with instrument measurement limitations, or incomplete numerical parameterizations, and propose forms for the continuation of these spectra, in order to properly estimate the Stokes drift. Depending on the instrument and the sea state, predictions of surface Stokes drift may be underestimated by more than 50%.

1. Introduction

Deep-water surface gravity waves play a crucial role in the marine boundary layer, modulating the exchange of mass, momentum, heat and gases between the ocean and the atmosphere (Melville, 1996; Cavaleri et al., 2012). Irrotational surface waves have particle orbits that are not closed, but instead are slightly elliptic, leading to a drift in their direction of wave propagation, know as Stokes drift. This drift is usually inferred from the directional surface wave spectrum (Kenyon, 1969). Accurately estimating the Stokes drift is critical for a number of applications; from the study of upper ocean and air-sea interaction processes, such as Langmuir circulations (Craik and Leibovich, 1976; Leibovich, 1983; McWilliams et al., 1997) that rely on a proper representation of the wave-induced drift (McWilliams and Restrepo, 1999; Belcher et al., 2012), to the prediction of the transport of pollutants, oil spills and drifting objects (see also Lenain et al., 2019a). Additionally, better evaluation of the Stokes drift may lead to an improved predictive capability of larger scale ocean dynamics (Shrira et al., 2020) that play a crucial role in weather and climate models (Breivik et al., 2019, among others).

In recent years, improvements in remote sensing and in-situ observational techniques have led to significant progress in our ability to measure and understand spatio-temporal properties of surface gravity waves. In Lenain and Melville (2017), properties of the directional distribution of the surface wave field across the equilibrium and saturation ranges (Phillips, 1985) were investigated from airborne lidar data (see also Melville et al., 2016). They demonstrated that the omnidirectional wavenumber spectra, $\phi(k)$, where k is the wavenumber, exhibits a consistent power-law behavior, proportional to $k^{-5/2}$ in the equilibrium range and k^{-3} in the saturation range, as predicted by Phillips (1985). These two regions of the wave spectrum have been extensively studied previously, both through theoretical analysis (see, for example, Phillips, 1958; Toba, 1973; Kitaigorodskii, 1983; Phillips, 1958), spatial and temporal in-situ observations (Donelan et al., 1985; Battjes et al., 1987; Hwang et al., 2000; Romero and Melville, 2010a; Melville et al., 2016, among others) and numerical investigation (Pushkarev et al., 2003; Romero and Melville, 2010b, amongst others) of the wind-generated wave field, but never with the broad spectral range required to fully capture and parameterize the transition from equilibrium to saturation ranges. These datasets of surface wave spectra offer us a unique opportunity to carefully investigate the impact of spectral shape, and specifically the high-frequency surface wave contribution, to the total Stokes drift.

Mixing in the upper ocean controls the transfer of heat, and trace gases, between the atmosphere and ocean. The heat content serves as an imporant boundary condition for coupled air-sea models of both weather and climate. Errors in estimates of these fluxes can lead to biases in sea surface temperature. In Belcher et al. (2012), it was shown that the inclusion of surface wave processes can reduce the sea surface temperature biases. This relies crucially on estimates of the turbulent Langmuir number, given by the ratio of the wind friction velocity to the Stokes drift. Therefore, it is critical to properly estimate the Stokes drift, which serves as the motivation for this paper.

Kenyon (1969), based on Phillips (1966), first related the wave energy spectrum to the Stokes drift. Since then, there has been considerable attention given to estimating the Stokes drift through a minimal number of environmental variables that characterize the wave spectrum, particularly in recent years (Breivik et al., 2016, 2014; Van Den Bremer and Breivik, 2018). The integral computations are subtle, as the directional distribution of the waves crucially modulates the total Stokes drift (Webb and Fox-Kemper, 2015), and one needs to resolve the small scale waves, which significantly contribute to the drift (Pizzo et al., 2019). Now, the directionality of the wave field, from the spectral peak to the realignment of the capillary waves with the longer gravity waves, is still a source of uncertainty, both in measurements and more severely in ocean wave models (Stopa et al., 2016; Liu et al., 2019). Furthermore, many studies employ the omnidirectional wave spectrum when computing the Stokes drift (McWilliams and Restrepo, 1999; Sullivan et al., 2007; Breivik et al., 2014). Therefore, in this paper we focus on omnidirectional wave spectrum effects, while a manuscript on the directional effects is currently in preparation.

Here, in addition to the observations presented in Lenain and Melville (2017), we also consider measurements collected during two additional field programs, the Langmuir and Innershelf ONR DRI field efforts (LCDRI2017 and ISDRI2017, respectively), providing a much broader range of environmental conditions which leads to a significantly improved parameterization of the transition between equilibrium and saturation ranges. This dataset provides a unique opportunity to characterize the contribution, across a broad range of scales, to the Stokes drift, and in turn, the error caused by the use of frequency-limited wave spectra or numerical wave spectra with an incorrect parameterization of the transition from equilibrium to saturation ranges.

2. Experiments, instrumentation, and environmental conditions

a. Experiments

The present study is based on data collected during three ONR funded programs: SOCAL2013, LCDRI2017 and ISDRI2017. The first two projects were focused on phase-resolved measurements of wind and waves. Observations over a broad range of environmental conditions were collected. Both of these experiments were located between San Clemente and San Nicholas Islands (vicinity of $33^o13.202'$N, $118^o58.767'$W) where the floating ocean research platform R/P FLIP was moored from November 7 to 22, 2013 and March 16 to April 10, 2017, for the SOCAL2013 and LCDRI2017 experiments, respectively. R/P FLIP was instrumented with a suite of meteorological sensors to characterize the atmospheric, surface and subsurface conditions at the experiment site. Data from the ISDRI2017 experiment were collected from September 5 to

21 2017 off the coast of Point Sal, CA. In that case, surface conditions were estimated from an airborne lidar, as described in Lenain et al. (2019b). Overall, the environmental conditions considered here have wind speeds ranging from 2 m/s to 13 m/s, and significant wave height H_s in the range of approximately 1 to 4 m.

b. The Modular Aerial Sensing System (MASS)

Spatio-temporal measurements of the sea surface topography and surface kinematics were collected from a Partenavia P68 aircraft that was instrumented with the Modular Aerial Sensing System (MASS), an instrument package developed at the Scripps Institution of Oceanography, as described in Melville et al. (2016). The instrument package is built around a Q680i waveform scanning lidar (Riegl, Austria), used to make spatio-temporal measurements of the sea surface elevation. The sensor has a maximum pulse repetition rate of 400 kHz, a maximum line scan rate of 200 Hz, and has been used at altitudes up to 1500 m with sufficient lidar pulse returns for surface-wave measurements. All data collected are carefully georeferenced from the aircraft to an Earth coordinate frame using a Novatel SPAN-LN200, a GPS-IMU system combining GPS technology with an IMU using fiber-optic gyros and solid-state accelerometers to provide position and attitude data at up to 200 Hz. After post-processing, we typically find absolute vertical errors of 2 to 4 cm (per lidar pulse) for the final topographic product (for more details, see Melville et al., 2016; Lenain and Melville, 2017; Lenain et al., 2019b).

c. Environmental conditions

During the SOCAL2013 and LCDRI2017 experiments, a suite of atmospheric sensors were installed on R/P FLIP's port boom to characterize the marine atmospheric boundary layer variables that are used in the present analysis. While the setup was slightly different in each experiment (see technical details in Grare et al. (2018) and Lenain et al. (2019b)), the friction velocity in the air was computed from a sonic anemometer (Gill R3-50) mounted on a vertical mast that was deployed from the end of the horizontally extended 20 m long port boom of FLIP in both experiments, using eddy correlation techniques. Here the friction velocity in the air, u_*, is given by

$$u_* = (\overline{u'w'}^2 + \overline{v'w'}^2)^{1/4}, \tag{1}$$

where u, v, w represent the three components of the wind vector in the along, cross and vertical directions, respectively, and the $'$ denotes deviations from the mean. The covariances $\overline{u'w'}$ and $\overline{v'w'}$ are computed over 30 minute records.

During the ISDRI experiment, the environmental conditions were estimated remotely using the MASS. Here the friction velocity u_* was computed using the method described in Lenain et al. (2019b).

3. Spectral depiction of wind-generated surface waves across the equilibrium-saturation ranges

Phillips (1985) proposed a model to describe the "equilibrium" range, based on the assumption of balance, proportionality and similar order of magnitude of the terms in the statistical equilibrium radiative transfer equation (namely wave-wave interactions, wind forcing and wave-breaking dissipation). Phillips's model predicts a $k^{-5/2}$ slope for the equilibrium range of the omnidirectional spectrum. Beyond the equilibrium range, spatial and temporal observations of wind waves show a power-law transition from a $k^{-5/2}$ to a k^{-3} slope corresponding to another regime, the so-called "saturation" range (Forristall, 1981; Banner, 1990; Romero and Melville, 2010a; Lenain and Melville, 2017). In that case, the primary balance is between the wind input and the dissipation from breaking waves, as the the time scales in this range are short enough such that nonlinear wave-wave interaction term becomes negligible. Observations of the transition between these two regimes is difficult, and our novel measurements over these ranges enabled this work.

a. Methods

Swaths of ocean topography collected from the MASS lidar were carefully georeferenced from the aircraft to an Earth-coordinate frame three dimensional point cloud. For SOCAL2013 and LCDRI2017, five-kilometer long swaths of data collected within 10km of R/P FLIP (where the atmospheric measurements were conducted) were gridded and interpolated on a regular grid, with the horizontal spatial resolution a function of the flight altitude: $dx = dy = 0.1$m for aircraft altitudes lower than 200m Above Mean Sea Level (AMSL), corresponding to a typical swath width of 50-150m, $dx = dy = 0.2$m for altitudes ranging from 200 to 400m AMSL, and $dx = dy = 1$m for higher altitudes (with a corresponding swath width of 400-800m). The data collected along the cross-track edges of the swath were discarded due to high dropout rates ($<$10-15% pulse returns). Two-dimensional fast Fourier transforms were computed over 5km segments with 50% overlap. All segments were first detrended, then tapered with a two-dimensional Hanning window and finally padded with zeros (25%).

To correct for the Doppler shift induced by the relative motion between the phase speed of the wave and the aircraft velocity, each spectrum was corrected iteratively following the method developed by Walsh et al. (1985). The change in wavenumber component in the along-track direction is taken as

$$\delta k_x = \frac{\omega}{v_a}, \tag{2}$$

where $\omega(k)$ (rad/s) is the radial wave frequency, computed from a deep-water dispersion relationship, and v_a (m/s) is the aircraft velocity in the along-track direction.

A similar approach was taken for the data collected during the ISDRI2017 experiment. In that case, as the operational area included very shallow to deep water, we only considered water depth h larger than 50 m.

We next introduce the *omnidirectional* wave spectrum, $\phi(k)$, defined as the azimuthally averaged directional spectrum,

$$\phi(k) = \int_0^{2\pi} F(k,\theta)\, kd\theta, \tag{3}$$

where $F(k,\theta)$ is the wave directional spectrum. Figure 1(a) shows an example of the azimuthally integrated omnidirectional spectrum computed from data collected during the SOCAL2013 experiment. The variable k_p represents the spectral peak wavenumber of the wind-generated waves. The separation at wavenumber k_n of the spectral slopes into -2.5 (equilibrium) and -3 (saturation) regions is clear and in this case the transition wavenumber k_n is found to be equal to 0.6 rad/m.

b. Improved parameterization of the equilibrium-saturation range transition

Part of the analysis presented in Lenain and Melville (2017) was dedicated to the characterization and parameterization of the transition wavenumber k_n. We expanded their work to include two additional field experiments, LCDRI2017 and ISDRI2017. For each azimuthally integrated spectrum the transition wavenumber, k_n, was computed by estimating the intersection between a $k^{-5/2}$ fit in the equilibrium range and a constant saturation value at higher wavenumbers, i.e k^{-3}. Results are presented in figure 1(b), where the transition wavenumber is plotted against g/u_*^2, a quantity introduced in Phillips (1985) to describe the upper end of the equilibrium spectrum such that r (sometimes referred to as Phillips's constant), a constant, is defined as

$$r = \frac{k_n u_*^2}{g}. \tag{4}$$

Here we find $r = 9.7 \times 10^{-3}$.

This result is of tremendous interest to the wave modeling community. While there has been growing recognition of the existence of equilibrium and saturation regimes, properly parameterizing their transition has been a challenge (Liu et al., 2019). Here we corroborate the parameterization proposed by Phillips (1985) for the transition from equilibrium to saturation ranges that only requires the friction velocity u_*, and therefore can be easily implemented in operational wave models.

4. Stokes drift

The Stokes drift is computed from the directional spectrum F, given by (Kenyon, 1969)

$$\mathbf{U}_s = 2\int\int F(\mathbf{k})\sqrt{gk}e^{2kz}\mathbf{k}d\mathbf{k}, \tag{5}$$

where $k = |\mathbf{k}|$ and z is the depth (i.e. z=0 at the surface).

Here, we define the Stokes drift magnitude $U_s(z)$ based on the omnidirectional wave spectrum $\phi(k)$, such that

$$U_s(z) = 2\int_{k_p}^{\infty} \phi(k)\sqrt{gk}e^{2kz}kdk, \tag{6}$$

where k_p is the peak wavenumber of the wind-waves, z the depth and $\phi(k)$ is the omnidirectional wave spectrum defined in equation (3). Hence, by definition the spectral shape of surface waves will have a direct impact on Stokes drift. Note, following Breivik et al. (2014) and Pizzo et al. (2019), we ignore the contribution to the Stokes drift of the very low wavenumbers (i.e. swell), as these waves are not steep so that their contribution to the total drift is very small.

Following equation (6), the Stokes drift is computed for all three experiments described in the previous section, and at seven set depths z: 0 (surface), -0.1, -0.2, -0.5, -1, -2, and -5m. Since the transition between saturation and equilibrium ranges are clearly characterized in the three datasets, we can compute the contribution of the equilibrium range to the total wind-generated surface Stokes drift, where the Stokes drift in the equilibrium range is defined as

$$U_{s,eq}(z) = 2\int_{k_p}^{k_n} \phi(k)\sqrt{gk}e^{2kz}kdk. \tag{7}$$

This is shown in figure 2, for $z = 0$m (surface), plotted against the friction velocity u_*. We find that as the friction velocity increases, the contribution of the equilibrium range decreases, reaching a plateau for u_* larger than 0.35 ms^{-1}, with a value of approximately 45 to 65 % of the total Stokes drift. In other words, the contribution from the high-frequency part of the surface wave spectrum, i.e. the saturation range, is not negligible when computing Stokes drift, especially at the surface, and needs to be fully resolved.

5. Contribution of the high-frequency wind-generated surface waves

In this section, we look at the impact of the cut-off frequency on the magnitude of the Stokes drift, effectively highlighting the significance of the contribution from the higher wavenumber part of the saturation spectra. This is particularly relevant, as Stokes drift is often computed using surface wave measurements without paying much attention to the frequency or wavenumber spectral range, and in particular the maximum frequency resolved.

For reference, directional wave buoys are generally able to resolve surface waves up to scales of approximately 0.5-0.6Hz, similar to what global reanalysis products, such as the ERA datasets (e.g. ERA-Interim or ERA5) from ECMWF, can now resolve (Uppala et al., 2005; Dee et al., 2011). It is clear from figure 1 that such cutoff frequencies are not adequate to resolve the Stokes drift contribution from the saturation range.

To quantify the errors associated with the use of surface wave spectra that do not resolve high enough frequencies to accurately compute Stokes drift, we introduce here $U_{s,nb}$, such that

$$U_{s,nb}(z) = 2\int_{k_p}^{k_c} \phi(k)\sqrt{gk}e^{2kz}k\,dk, \tag{8}$$

where k_c is a cutoff frequency.

We compute the error (i.e. underestimation) associated with an inadequate cutoff frequency f_c in estimating U_s such that

$$\text{error} = 100 \times \frac{|U_s(z) - U_{s,nb}(z)|}{U_s(z)}. \tag{9}$$

Figure 3 shows the surface (z=0) Stokes drift error defined in equation (9) computed for cutoff frequencies f_c ranging from 0.3 to 1.8Hz (i.e. 0.36 to 13 rad/m). We find the error rapidly decreases as f_c increases, following an exponential decay (dash line), such that

$$\text{error} = ae^{-bf_c}, \tag{10}$$

where a is equal to 133.15 and b, the e-folding scale, is 2.47, estimated through a least-squared fit (r^2=0.99). This simple relationship can be used to correct surface Stokes drift estimates computed from spectrally limited in-situ observations or reanalysis products.

For reference, the cutoff frequency of commonly used spectral wave products is also shown, the ECMWF ERA40 [1] and ERA5 reanalysis global datasets (Uppala et al., 2005; Dee et al., 2011), and buoy-based observations from the CDIP network (`https://cdip.ucsd.edu/`). We find that computing Stokes drift from these products alone would lead to significant underestimations, ranging from approximately 50% error for ERA40, 35% for ERA5, and down to 34% for the CDIP wave products.

Moreover, it is sometimes assumed that the high-frequency part of the surface wave field does not contribute to the Stokes drift at depth, even close to the surface. This is investigated in figure 4(a), where the Stokes drift error is shown for depths ranging from the surface down to 5m. As expected, as depth increases, the contribution of the shorter waves to the Stokes drift is reduced. At 5m depth, we find that the contribution from waves of frequencies larger than 0.4Hz is negligible. Nevertheless, and this is of importance for upper ocean modeling, the contribution from

[1] The reanalysis product used in Belcher et al. (2012).

shorter waves, of frequencies larger than for example ERA5 products (0.5478Hz) or in-situ observations (0.4-0.5Hz at best), is not negligible above 5m depth, and increases rapidly closer to the surface. Figure 4(b) shows the depth-dependent term of the Stokes drift in equation (7), e^{2kz}, plotted against cutoff frequency, another way of illustrating the penetration depth of short waves and their contribution to the total Stokes drift. Finally, we note that although the contribution of the short waves to the Stokes drift attenuates rapidly with depth, their shear values are large, so that we expect them to be an important contribution to the turbulent kinetic energy budget (see, for example, equation 1 of Belcher et al., 2012).

Ultimately, this result provides guidance on the contribution of high frequency surface waves to horizontal wave induced transport in the upper ocean, particularly near the ocean surface.

6. Is adding a spectral tail to limited bandwidth spectra sufficient?

An approach to mitigating the availability of limited-bandwidth wave spectra when computing Stokes drift has been to add a high-frequency spectral tail of set slope (i.e. f^{-5} or k^{-3}) to the spectrum (see for example Belcher et al., 2012), or extrapolating a wave spectrum to a set saturation level (Romero et al., 2012). Here we attempt to evaluate this method using the broad bandwidth wave spectra that were collected during the three field programs with the MASS lidar instrument.

In figure 5, we compare the intentionally frequency-limited estimate of the surface Stokes drift $U_{s,nb}(z=0)$, where k_c is set here to 0.67 rad/m (i.e. f_c = 0.41Hz), corresponding to the cutoff frequency of ERA40 used in Belcher et al. (2012), to the ”true” Stokes drift (red dots), computed from the full omnidirectional spectra collected during the three experiments[2]. The dashed line represents 1:1, while the white circles represent bin-averaged values. As discussed in the prior

[2]For reference, the maximum wavenumber resolved in the field observations is approximately 13 rad/m.

section, the need for including high frequencies in the computation of the Stokes drift is obvious here, as we found underestimation of close to 50% at times when they were not included.

Following Belcher et al. (2012), we also applied a saturation tail (f^{-5} or k^{-3}) to the frequency-limited spectra for frequencies larger than k_c (gray dots, figure 5). While the Stokes drift that was estimated using the k^{-3} tail show good agreement for large U_s, we nevertheless find that this approach underestimates the surface Stokes drift by $10-30\%$ for smaller values of U_s, in the 0.075-0.15 m/s range. This brings up the importance of properly characterizing the spectral shape of the wave spectrum described in an earlier section. As shown in figure 6, depending on the cutoff frequency k_c relative to the transition wavenumber k_n, applying a set slope tail to the spectra will have very different outcomes. When $k_c > k_n$, we find the surface Stokes drift to be properly estimated. However, when $k_c < k_n$, the transition from equilibrium to transition regimes effectively is forced to k_c, in turn truncating the contribution of the high frequency part of the wave spectrum to the Stokes drift, as highlighted in figure 6.

7. Errors caused by the misrepresentation of the transition between the equilibrium and saturation ranges

Misrepresentation of the transition between the equilibrium and saturation ranges is another potential source of errors when computing Stokes drift. To characterize this effect, we make use of an updated version of the model of surface Stokes drift from Pizzo et al. (2019). The model has been validated with field observations, showing remarkable agreement with the estimates computed from observed wave spectra using equation (6), as described in the Appendix. Here we use the model over the range of environmental parameters observed during the three experiments, and artificially vary the transition wavenumber k_n, defined here as $k_{n,est}$, and compare the resulting Stokes drift to the one computed with the accurate k_n. Results are shown in figure 7. This demonstrates the need to pay particular attention to the spectral shape of the surface wave spectra used in Stokes drift computations. For example, a factor two underestimation of k_n leads to a 15% error in surface Stokes drift estimate, which is significant.

8. A practical example: Stokes drift and turbulent Langmuir number from in-situ buoy measurements

To highlight the findings presented in the prior sections, we used publicly available data collected from a NDBC station located in the Gulf of Mexico (42040). This buoy is equipped with both wind and surface wave measurement capabilities, and is located at 29.208 N 88.226 W. More details about about this station can be found on the NDBC website (`https://www.ndbc.noaa.gov/station_page.php?station=42040`).

Here, the surface Stokes drift is computed in three different ways. First using the original, limited bandwidth surface wave spectrum provided by NDBC (f=0.02-0.485 Hz), i.e. no corrections applied, and two other versions that include a high frequency spectral tail: one case where a f^{-5} saturation tail is added for $f > 0.485Hz$, and a second version where the spectra are patched with an equilibrium f^{-4} and saturation f^{-5} tails for cases where the transition frequency $f_n = \sqrt{gk_n}/2\pi$ is larger than 0.485Hz. for the latter, k_n is computed using equation (4) with r taken as 9.7e-3. The maximum frequency of the high-frequency tail $f_M = \sqrt{gk_M}/2\pi$ is defined as the cutoff wavenumber above which the directional wave spectrum is assumed isotropic, based on the findings of Lenain and Melville (2017), such that $k_M = u_*^2/g\ exp((\pi/2-\theta_0)/\gamma)$, where $\theta_0 = 2.835$ and $\gamma = 0.48$ (see equation (4) of Lenain and Melville, 2017, for details).

Results are presented in figure 8, showing data collected from NDBC 42040 from April 2017 through January 2018. The top panel (a) shows the wind speed collected at z=3.8m from the buoy, and (b) the surface Stokes drift, as described above. As expected from the previous sections, we find the Stokes drift to be significantly underestimated when no spectral tail is added. We also find that properly parameterizing the transition from equilibrium to saturation ranges in the spectral tail also has significant impact, particularly for U_s smaller than 0.1 m/s. This is highlighted in figure 8(c) where the Stokes drift estimates are shown over a shorter period of time (September 2017). The two estimates with spectral tail added collapse for higher winds (in that case $f_n < f_c = 0.485 Hz$), around September 10 2017, while significant differences are found as the wind decreases, after September 13 2017.

Next, recall that upper ocean mixing is parameterized through the turbulent Langmuir number (McWilliams et al., 1997), defined as

$$La_t = \sqrt{\frac{u_{*w}}{u_s}}, \tag{11}$$

where u_{*w} is the friction velocity in the water such that $u_{*w} = \sqrt{\tau \rho_w}$, ρ_w the water density and τ the surface stress. As this parameter is used in both weather and climate models to parametrize mixing and the heat content in the upper ocean, it is critical to ensure that this quantity is computed correctly. Figure 9 shows the turbulent Langmuir number computed for the data presented in figure 8(c). As anticipated, the addition of a spectral tail significantly reduces La_t. What is less expected is the sensitivity of the turbulent Langmuir number to the shape of the spectral tail. Specifically, we find that if the transition frequency between equilibrium and saturation ranges is not parameterized correctly, La_t can be overestimated by up to 30-40%, which may lead to significant biases in sea surface temperatures (Belcher et al., 2012).

9. Discussion

In this paper, we provide a better description of the spectral evolution of wind-generated waves. Specifically, we expand the work of Lenain and Melville (2017) on the partitioning into equilibrium and saturation ranges of surface gravity waves, as originally proposed by Phillips (1985), using high resolution measurements of wind-generated surface gravity waves. In particular, we propose a simple parameterization of the transition from equilibrium to saturation regimes of wind-generated surface gravity waves, only requiring the atmospheric friction velocity u_* as input, that could be readily implemented in wave models. This is significant, as currently most operational models do not explicitly parameterize this transition (Liu et al., 2019).

Error analysis was performed to quantify the errors in the estimated Stokes drift, as a function of cut-off frequency and transition wavenumber. It is found that there might be significant under-estimation (exceeding 50%) in estimates of Stokes drift based on instrument or reanalysis product limitations. Importantly, we provide an explanation for why this occurs and offer a means of correcting Stokes drift when only spectrally limited data is available. We identify that the misrepresentation of the transition from equilibrium to saturation ranges has an impact on the estimate of Stokes drift computed spectrally. While the analysis is mostly focused here on surface Stokes drift, where we anticipate the contribution of the shorter waves to be largest, depth dependence is also investigated, to provide guidance on the contribution of surface waves to horizontal transport in the upper ocean, near the ocean surface.

The Stokes drift plays a crucial role in upper ocean dynamics, via interactions with existing vorticity through the so-called vortex force term (Leibovich, 1983). This mixes the upper ocean, and sets the boundary conditions for coupled air-sea models. Estimates of the mixing is parameterized through the Langmuir number, a ratio of the wind friction velocity to the Stokes drift (Belcher et al., 2012). As this parameter is used in both weather and climate models, it is crucial to have high fidelity observations of this quantity. The work done in this paper provides better estimates of the Stokes drift, and hence better estimates of the turbulent Langmuir number to be used in these coupled models. The sensitivity of this number to the spectral estimate of Stokes drift was demonstrated here.

Finally, the directionality of the wave field is still a source of uncertainty both in measurements and more significantly in ocean wave models, and is the focus of on-going studies. Nevertheless, the emphasis in the present work on the need to include high-frequency waves, and to properly parameterize the equilibrium-saturation range transition in limited-bandwidth wave products also directly applies to directional surface wave estimates of the Stokes drift.

Acknowledgments. The authors gratefully acknowledge numerous discussions with Ken Melville on this topic prior to his passing in the fall of 2019. The authors are grateful to Aspen Helicopter for providing flight resources. We are thank Laurent Grare for providing the atmospheric data collected from R/P FLIP and for helpful discussions, and Nick Statom for his support during the field experiments and in the analysis of the lidar data. This research was supported by grants from the Physical Oceanography programs at ONR (Grants N00014-17-1-2171, N00014-14-1-0710, and N00014-17-1-3005) and NSF (OCE; Grant OCE-1634289). Data availability: All presented data are available at the UCSD Library Digital Collection (`https://library.ucsd.edu/dc`).

APPENDIX

A1. Stokes Drift Model

Here we revisit the model of the Stokes drift from Pizzo et al. (2019) to validate it using field observations of the directional wave spectrum collected during three experiments (SOCAL2013, LCDRI2017, ISDRI2017). In addition to the model considered there, we add a high wavenumber maximum, k_M, above which we assume the waves do not contribute to the Stokes drift. The maximum wavenumber k_M is defined as the cutoff wavenumber above which the directional wave spectrum is assumed isotropic, based on the findings of Lenain and Melville (2017), such that $k_M = u_*^2/g\ exp((\pi/2 - \theta_0)/\gamma)$, where $\theta_0 = 2.835$ and $\gamma = 0.48$ (see equation (4) of Lenain and Melville, 2017, for details). As the Stokes drift goes like $\phi(k)k^{3/2}$, particular care is needed in where to place this cutoff (Breivik et al., 2014), and is discussed in more detail below.

With this addition, following Pizzo et al. (2019), the Stokes drift U_s at the surface (z=0) can be shown to scale as

$$U_s = \beta u_* ln\left(\frac{rg}{u_*^2}\frac{1}{k_p}\right) + 4B\left(\frac{u_*}{r^{1/2}} - \sqrt{\frac{g}{k_M}}\right), \tag{A1}$$

where B is the saturation constant, given a saturation spectra Bk^{-3} (see figure 1), set to 7×10^{-3} in the present study, based on the findings of Lenain and Melville (2017), and β is an empirical parameter, often referred to as Toba's constant (Toba, 1973) that can be computed directly from the equilibrium range of wind generated surface waves such that

$$\phi(k) = \frac{\beta}{2}\frac{u_*}{\sqrt{g}}k^{-5/2}. \tag{A2}$$

While it is defined here as a constant, Resio et al. (2004) and Romero and Melville (2010a) introduced a weak dependence of β on the wave phase speed at the spectral peak, and effective wave age, respectively.

Figure 10(a) shows the modeled surface Stokes drift computed from equation (A1) compared to the Stokes drift computed explicitly using the measured omnidirectional spectra as described in equation (7) for z=0. The dashed line shows a 1:1 ratio. We find good agreement between the model and measured Stokes drift, with a coefficient of determination R^2 of 0.78. Note that by setting Toba's constant to 0.105, and in turn to avoid the need for a measurement of the compensated wave spectrum or another parameterization for this variable, we find, not unexpectedly, more scatter, but nevertheless a reasonable agreement with $R^2 = 0.58$.

Next, following Pizzo et al. (2019), we can rewrite equation (A1) in terms of the spectrally weighted phase velocity c_{pm} such that

$$U_s = \beta u_* ln\left(2r\frac{c_{pm}^2}{u_*^2}\right) + 4B\left(\frac{u_*}{r^{1/2}} - \sqrt{\frac{g}{k_M}}\right). \tag{A3}$$

Here c_{pm} is defined following Sutherland and Melville (2015), in an attempt to better represent the wind-wave portion of the spectrum, as describing a broad, wind generated wave field only using a peak frequency has significant limitations (Lenain and Melville, 2017). Results are presented in figure 10(b); we find a very good agreement between the proposed model and the surface Stokes drift computed from the wave spectra, with a R^2 value of 0.88, much better than what was found using equation (A1).

Note, there is a factor of two missing in the drift estimates Pizzo et al. (2019), which is now corrected in equations (A1) and (A3). This did not affect their scaling relationships, as an arbitrary constant was involved in each of the distinct regimes (e.g. equilibrium and saturation ranges).

References

Banner, M. L., 1990: Equilibrium spectra of wind waves. *Journal of Physical Oceanography*, **20 (7)**, 966–984.

Battjes, J., T. Zitman, and L. Holthuusen, 1987: A reanalysis of the spectra observed in jonswap. *Journal of Physical Oceanography*, **17 (8)**, 1288–1295.

Belcher, S. E., and Coauthors, 2012: A global perspective on langmuir turbulence in the ocean surface boundary layer. *Geophysical Research Letters*, **39 (18)**.

Breivik, Ø., J.-R. Bidlot, and P. A. Janssen, 2016: A stokes drift approximation based on the phillips spectrum. *Ocean Modelling*, **100**, 49–56.

Breivik, Ø., A. Carrasco, J. Staneva, A. Behrens, A. Semedo, J.-R. Bidlot, and O. J. Aarnes, 2019: Global stokes drift climate under the rcp8. 5 scenario. *Journal of Climate*, **32 (6)**, 1677–1691.

Breivik, Ø., P. A. Janssen, and J.-R. Bidlot, 2014: Approximate Stokes drift profiles in deep water. *Journal of Physical Oceanography*, **44 (9)**, 2433–2445.

Cavaleri, L., B. Fox-Kemper, and M. Hemer, 2012: Wind waves in the coupled climate system. *Bulletin of the American Meteorological Society*, **93 (11)**, 1651–1661.

Craik, A., and S. Leibovich, 1976: A rational model for Langmuir circulations. *Journal of Fluid Mechanics*, **73 (03)**, 401–426.

Dee, D. P., and Coauthors, 2011: The era-interim reanalysis: Configuration and performance of the data assimilation system. *Quarterly Journal of the royal meteorological society*, **137 (656)**, 553–597.

Donelan, M. A., J. Hamilton, and W. Hui, 1985: Directional spectra of wind-generated waves. *Philosophical Transactions of the Royal Society of London A: Mathematical, Physical and Engineering Sciences*, **315 (1534)**, 509–562.

Forristall, G. Z., 1981: Measurements of a saturated range in ocean wave spectra. *Journal of Geophysical Research: Oceans*, **86 (C9)**, 8075–8084.

Grare, L., L. Lenain, and W. K. Melville, 2018: Vertical profiles of the wave-induced airflow above ocean surface waves. *Journal of Physical Oceanography*, **48 (12)**, 2901–2922.

Hwang, P. A., D. W. Wang, E. J. Walsh, W. B. Krabill, and R. N. Swift, 2000: Airborne measurements of the wavenumber spectra of ocean surface waves. part i: Spectral slope and dimensionless spectral coefficient*. *Journal of Physical Oceanography*, **30 (11)**, 2753–2767.

Kenyon, K. E., 1969: Stokes drift for random gravity waves. *Journal of Geophysical Research*, **74 (28)**, 6991–6994.

Kitaigorodskii, S., 1983: On the theory of the equilibrium range in the spectrum of wind-generated gravity waves. *Journal of Physical Oceanography*, **13 (5)**, 816–827.

Leibovich, S., 1983: The form and dynamics of langmuir circulations. *Annual Review of Fluid Mechanics*, **15 (1)**, 391–427.

Lenain, L., and W. K. Melville, 2017: Measurements of the directional spectrum across the equilibrium saturation ranges of wind-generated surface waves. *Journal of Physical Oceanography*, **47 (8)**, 2123–2138.

Lenain, L., N. Pizzo, and W. K. Melville, 2019a: Laboratory studies of lagrangian transport by breaking surface waves. *Journal of Fluid Mechanics*, **876**.

Lenain, L., N. M. Statom, and W. K. Melville, 2019b: Airborne measurements of surface wind and slope statistics over the ocean. *Journal of Physical Oceanography*, **(2019)**.

Liu, Q., W. E. Rogers, A. V. Babanin, I. R. Young, L. Romero, S. Zieger, F. Qiao, and C. Guan, 2019: Observation-based source terms in the third-generation wave model wavewatch iii: updates and verification. *Journal of Physical Oceanography*, **49 (2)**, 489–517.

McWilliams, J. C., and J. M. Restrepo, 1999: The wave-driven ocean circulation. *Journal of Physical Oceanography*, **29 (10)**, 2523–2540.

McWilliams, J. C., P. P. Sullivan, and C.-H. Moeng, 1997: Langmuir turbulence in the ocean. *Journal of Fluid Mechanics*, **334**, 1–30.

Melville, W. K., 1996: The role of surface wave breaking in air-sea interaction. *Annual Review of Fluid Mechanics*, **28**, 279–321.

Melville, W. K., L. Lenain, D. R. Cayan, M. Kahru, J. P. Kleissl, P. Linden, and N. M. Statom, 2016: The modular aerial sensing system. *Journal of Atmospheric and Oceanic Technology*, **33 (6)**, 1169–1184.

Phillips, O., 1966: The dynamics of the upper ocean, cambridge univ. press. *New York*.

Phillips, O., 1985: Spectral and statistical properties of the equilibrium range in wind-generated gravity waves. *Journal of Fluid Mechanics*, **156 (1)**, 505–31.

Phillips, O. M., 1958: The equilibrium range in the spectrum of wind-generated waves. *Journal of Fluid Mechanics*, **4 (04)**, 426–434.

Pizzo, N., W. K. Melville, and L. Deike, 2019: Lagrangian transport by nonbreaking and breaking deep-water waves at the ocean surface. *Journal of Physical Oceanography*, **49 (4)**, 983–992.

Pushkarev, A., D. Resio, and V. Zakharov, 2003: Weak turbulent approach to the wind-generated gravity sea waves. *Physica D: Nonlinear Phenomena*, **184 (1)**, 29–63.

Resio, D. T., C. E. Long, and C. L. Vincent, 2004: Equilibrium-range constant in wind-generated wave spectra. *Journal of Geophysical Research: Oceans*, **109 (C1)**, doi:10.1029/2003JC001788, c01018.

Romero, L., and W. K. Melville, 2010a: Airborne observations of fetch-limited waves in the Gulf of Tehuantepec. *Journal of Physical Oceanography*, **40 (3)**, 441–465.

Romero, L., and W. K. Melville, 2010b: Numerical modeling of fetch-limited waves in the Gulf of Tehuantepec. *Journal of Physical Oceanography*, **40 (3)**, 466–486.

Romero, L., W. K. Melville, and J. M. Kleiss, 2012: Spectral energy dissipation due to surface wave breaking. *Journal of Physical Oceanography*, **42 (9)**, 1421–1444.

Shrira, V. I., R. B. Almelah, and Coauthors, 2020: Upper-ocean ekman current dynamics: a new perspective. *Journal of Fluid Mechanics*, **887**.

Stopa, J. E., F. Ardhuin, A. Babanin, and S. Zieger, 2016: Comparison and validation of physical wave parameterizations in spectral wave models. *Ocean Modelling*, **103**, 2–17.

Sullivan, P. P., J. C. McWILLIAMS, and W. K. Melville, 2007: Surface gravity wave effects in the oceanic boundary layer: Large-eddy simulation with vortex force and stochastic breakers. *Journal of Fluid Mechanics*, **593**, 405–452.

Sutherland, P., and W. K. Melville, 2015: Field measurements of surface and near-surface turbulence in the presence of breaking waves. *Journal of Physical Oceanography*, **45 (4)**, 943–965.

Toba, Y., 1973: Local balance in the air-sea boundary processes. *Journal of the Oceanographical Society of Japan*, **29 (5)**, 209–220.

Uppala, S. M., and Coauthors, 2005: The era-40 re-analysis. *Quarterly Journal of the Royal Meteorological Society: A journal of the atmospheric sciences, applied meteorology and physical oceanography*, **131 (612)**, 2961–3012.

Van Den Bremer, T., and Ø. Breivik, 2018: Stokes drift. *Philosophical Transactions of the Royal Society A: Mathematical, Physical and Engineering Sciences*, **376 (2111)**, 20170 104.

Walsh, E., D. Hancock III, D. Hines, R. Swift, and J. Scott, 1985: Directional wave spectra measured with the surface contour radar. *Journal of Physical Oceanography*, **15 (5)**, 566–592.

Webb, A., and B. Fox-Kemper, 2015: Impacts of wave spreading and multidirectional waves on estimating stokes drift. *Ocean Modelling*, **96**, 49–64.

LIST OF FIGURES

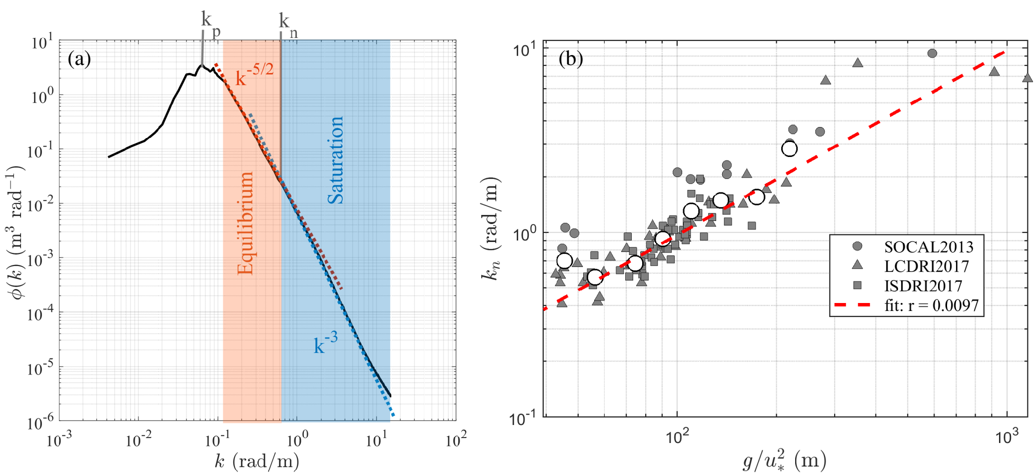

FIG. 1. (a) Example of the omnidirectional wavenumber spectrum collected on 15 November 2013 during the SOCAL2013 experiment using observations collected from an airborne topographic scanning lidar (Lenain and Melville, 2017). Note the presence of both equilibrium and saturation ranges, showing both -5/2 and -3 spectral slopes over the three-decade bandwidth of the data. (b) Transition wavenumber k_n plotted against g/u_*^2 for three experiments (SOCAL2013, LCDRI2017 and ISDRI2017). Phillips's (1985) parameter $r = k_n u_*^2/g$ is best fit to the data (red dashed line), and is equal to $r = 9.7 \times 10^{-3}$. The white circles represent bin-averaged values.

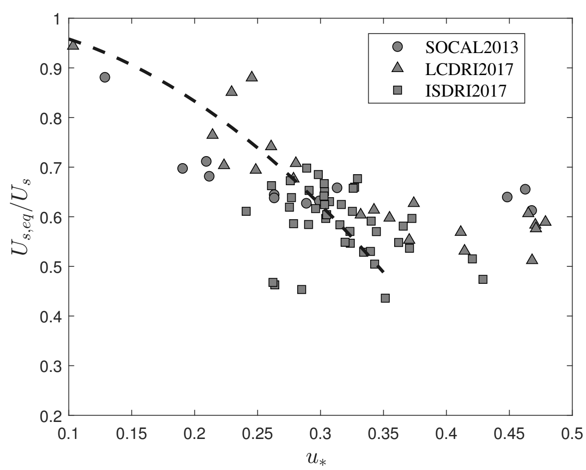

FIG. 2. Contribution of the equilibrium range to the total surface Stokes drift U_s at $z = 0$m. Here the Stokes drift is computed from equations (6) and (7). As the friction velocity increases, the contribution of the equilibrium range decreases, reaching a plateau for u_* larger than 0.35 m/s. A fit to the data (dashed line) is also shown, such that $u_{s,eq}/u_s = 1 - \alpha u_*^2$, where $\alpha = 4.18$.

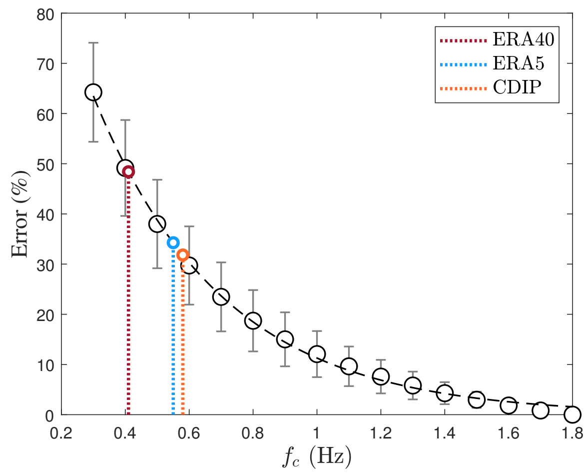

FIG. 3. Bin-averaged Surface Stokes drift estimated error as a function of cutoff frequency f_c computed from the surface wave spectra collected during all three experiments. Also shown are the current cutoff frequencies for wave spectral products, ECMWF ERA40, ERA5 and CDIP (observations), and errorbars for each bin of frequency.

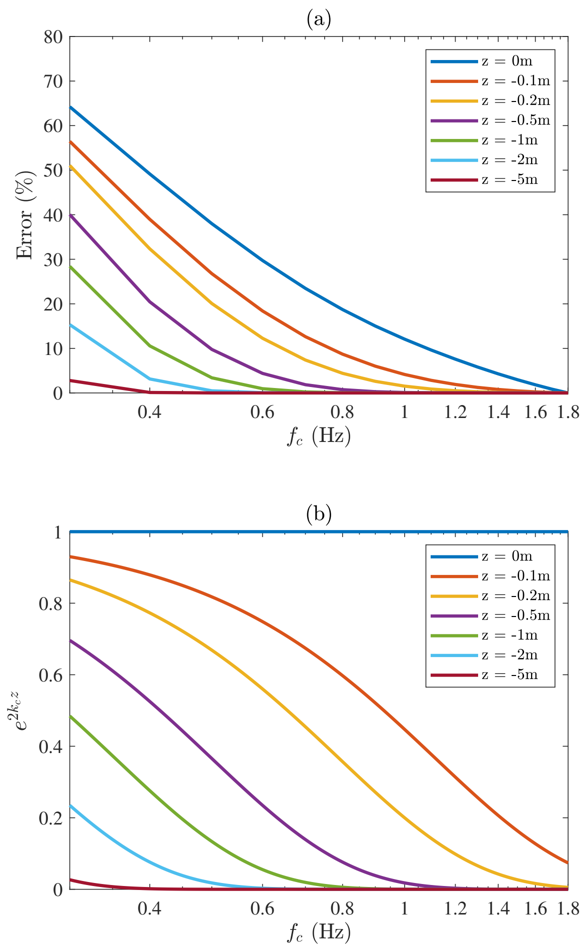

FIG. 4. (a) Stokes drift estimated error as a function of cutoff frequency f_c and depth (down to -5m) computed from the spectra of surface wave data collected during the three experiments. (b) Depth-dependence of the Stokes drift $e^{2k_c z}$ plotted against cutoff frequency. Below 5m depth, the contribution to the Stokes drift from waves of frequencies larger than 0.4Hz is negligible.

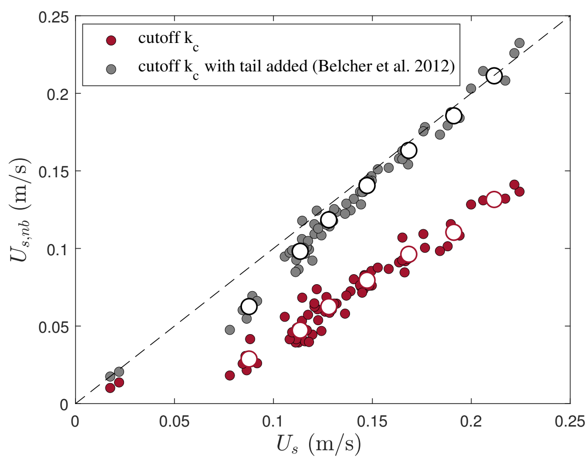

571 FIG. 5. The surface Stokes drift computed spectrally using a cutoff wavenumber k_c=0.67 rad/m, the highest ECMWF ERA40 resolved frequency (red), and taking a similar approach to Belcher et al. (2012), where they patched a saturation tail (f^{-5} or k^{-3}) for frequencies larger than k_c, plotted against the "true" Stokes drift U_s computed over the complete wavenumber range of the measured spectra. Here all three experiments are considered. The dashed line represents 1:1, while the white circles represent bin-averaged values. While the U_s estimates when patching a k^{-3} tail show good agreement for large U_s - this is expected, since $k_n < k_c$ in that case - we find that this approach underestimates the Stokes drift by $10-30\%$ for smaller U_s, in the 0.075-0.15 m/s range. Finally, the need for patching a tail when wave spectra that are computed explicitly do not resolve the high wavenumbers is obvious.

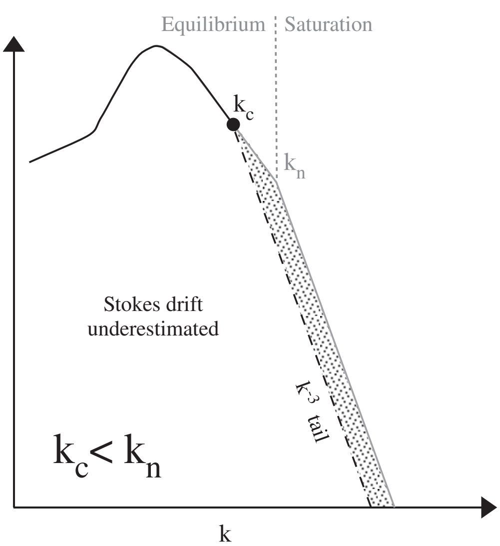

FIG. 6. Impact of adding a tail to limited bandwidth wave spectrum. (Left) $k_c < k_n$ and (right) $k_c > k_n$.

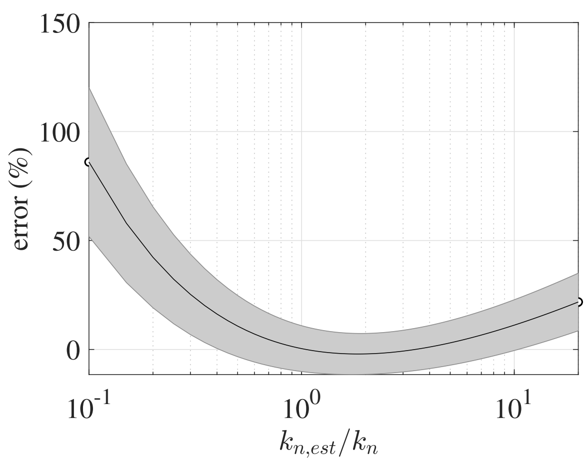

FIG. 7. Effect of the transition wavenumber k_n on the total Stokes drift, combining the three available data sets. Here k_n is the measured transition wavenumber, while $k_{n,est}$ is the one used to compute U_s from equation (A3). Errors are computed relative to the "true" Stokes drift, computed from the azimuthally integrated spectrum $\phi(k)$.

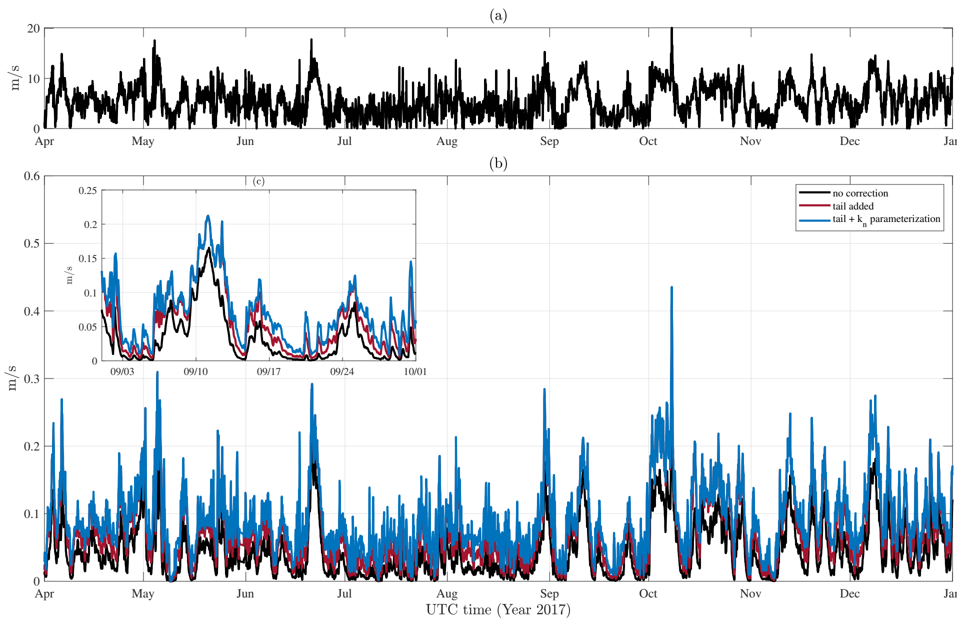

FIG. 8. (a) Wind speed (m/s) collected from NDBC buoy 42040 in the Gulf of Mexico in 2017. (b) Surface Stokes drift, computed using the measured wave spectra, along with two products that include a high frequency spectral tail: The red line shows the surface Stokes drift with a f^{-5} saturation tail, while the blue one is patched with an equilibrium f^{-4} and saturation f^{-5} tails for cases where the wave spectrum cutoff frequency is lower than $f_n = \sqrt{gk_n}/(2\pi)$. In that latter case, k_n is computed using equation (4) with r=9.7e-3. A shorter length of the record is also shown in (c), highlighting the significant differences in Stokes drift magnitude between each version. Also note that, as expected from the previous section, the two products with tail added collapse for higher winds, around September 10 2017, while significant differences are found as the wind decreases, after September 13 2017.

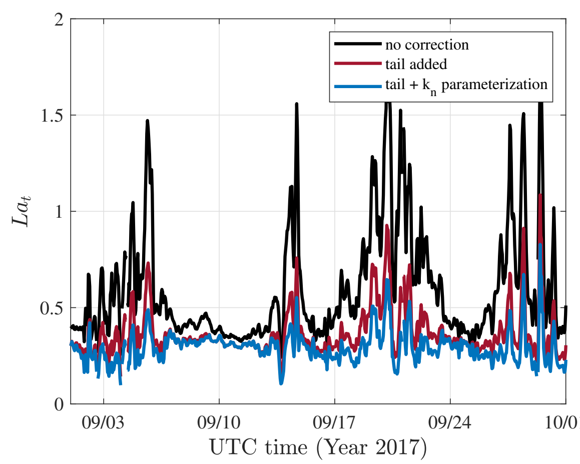

593 FIG. 9. Turbulent Langmuir number La_t for the same time period displayed in figure 8(c). Note the significant differences found between the three versions, and the significant overestimation of La_t when using the original, non-corrected surface wave spectrum from NDBC.

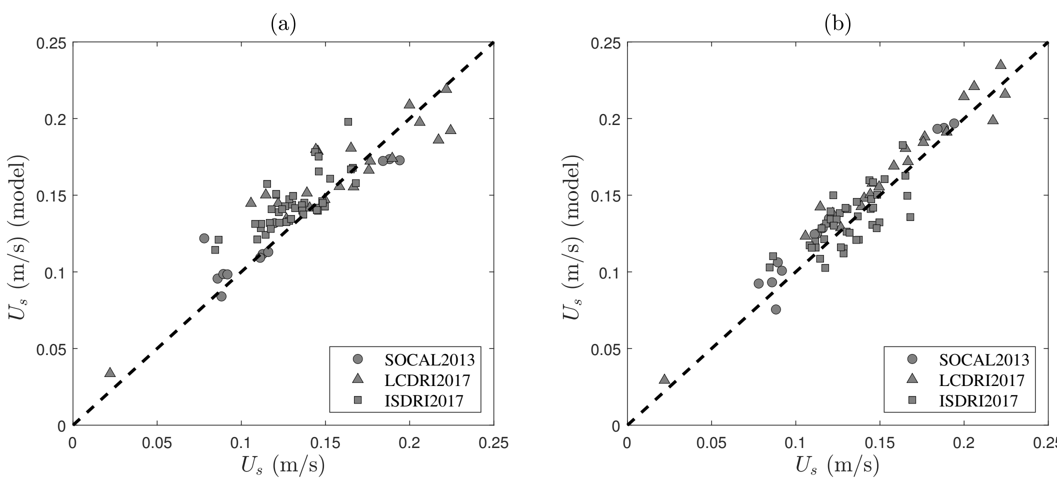

FIG. 10. (a) Surface Stokes drift computed from equation (A1), plotted against the Stokes drift computed from the azimuthally integrated spectra (equation 7) for the three experiments considered here. The dashed line represents 1:1. We see that there is good agreement between the model and the full prediction of the Stokes drift. The same comparison is shown in (b), this time using equation (A3).